

Directed crystalline symmetry transformation of blue-phase liquid crystals by reverse electrostriction

Received: 20 April 2024

Accepted: 6 August 2024

Published online: 15 August 2024


 Check for updates

Tsung-Hsien Lin¹ , Duan-Yi Guo¹, Chun-Wei Chen², Ting-Mao Feng¹, Wen-Xin Zeng¹, Po-Chang Chen¹, Liang-Ying Wu¹, Wen-Ming Guo¹, Li-Min Chang¹, Hung-Chang Jau¹, Chun-Ta Wang¹, Timothy J. Bunning³ & Iam Choon Khoo⁴ 

Soft-matter-based photonic crystals like blue-phase liquid crystals (BPLC) have potential applications in wide-ranging photonic and bio-chemical systems. To date, however, there are limitations in the fabrication of large monocrystalline BPLCs. Traditional crystal-growth process involves the transition from a high-temperature disordered phase to an ordered (blue) phase and is generally slow (takes hours) with limited achievable lattice structures, and efforts to improve molecular alignment through post-crystallization field application typically prove ineffective. Here we report a systematic study on the molecular self-assembly dynamics of BPLC starting from a highly ordered phase in which all molecules are unidirectionally aligned by a strong electric field. We have discovered that, near the high-temperature end of the blue phase, if the applied field strength is then switched to an intermediate level or simply turned off, large-area monocrystalline BPLCs of various symmetries (tetragonal, orthorhombic, cubic) can be formed in minutes. Subsequent temperature tuning of the single crystal at a fixed applied field allows access to different lattice parameters and the formation of never-before-seen monoclinic structures. The formed crystals remain stable upon field removal. The diversity of stable monocrystalline BPLCs with widely tunable crystalline symmetries, band structures, and optical dispersions will significantly improve and expand their application potentials.

Photonic crystals offer versatile platforms for fundamental research and diverse applications across physics, biology, and engineering. Their unique optical properties (such as spectrally selective transmission/reflection and strong dispersion), arising from periodic variations of refractive index, have spurred continuous efforts to fabricate larger and more varied crystalline symmetries^{1–10}. In contrast to conventional top-down methods (e.g., electron-beam writing and holographic lithography)^{1–6}, bottom-up approaches based on self-assembly of soft matter systems^{7–10}, including colloids, polymers, and liquid crystals,

have proven to be a scalable, cost-effective, relatively fast route to fabricating large photonic crystals across a broader spectral range, including the challenging ultraviolet regime. Among soft matters, liquid crystals, in various ordered phases, are particularly attractive. They are endowed with extraordinary properties such as large birefringence, transparency over a very broad spectrum, and susceptibilities to external stimuli (e.g., voltage, light, and even biological molecules) for dynamically modulating their properties or sensing. Naturally, therefore, liquid-crystalline photonic crystals, especially in

¹Department of Photonics, National Sun Yat-sen University, Kaohsiung 804201, Taiwan. ²Edward L. Ginzton Laboratory, Stanford University, Stanford, CA 94305, USA. ³Materials and Manufacturing Directorate, Air Force Research Laboratory, Wright-Patterson Air Force Base, Dayton, OH 45433, USA. ⁴Department of Electrical Engineering, The Pennsylvania State University, University Park, PA 16802, USA.  e-mail: jameslin@mail.nsysu.edu.tw; ick1@psu.edu

their 3D forms (e.g., blue-phase liquid crystals), have become a subject of intensive studies by material scientists, physicists and optical/photonics practitioners in fundamental pursuits as well as in wide-ranging applications from chemical and biological sensing to electro-optic display, switches, modulators, and nonlinear optics^{11–28}.

Blue-phase liquid crystals^{11,22,26,28} (BPLC) are usually made by incorporating chiral agents in nematics and enclosed in glass cells (see Section *Methods* for details in materials and cell assembly). BPLC typically exhibits isotropic liquid phase, blue phase II (BPII), blue phase I (BPI), and cholesteric phase in the order of decreasing temperature. With sufficiently strong chirality, molecules in the blue phases are self-assembled into double-twist cylinders (DTC)^{18,22,26,28}. These DTCs are periodically packed in a 3D network of line defects (inset in Fig. 1a) to form body-centered-cubic (BCC) lattices in BPI or simple-cubic lattices in BPII, in the absence of applied fields^{18,22,26,28}. These lattices exhibit periods of a few hundred nanometers, forming chiral photonic crystals with Bragg reflections of circularly polarized light across ultraviolet, visible, and near infrared regimes^{11,22,26,28}. They also exhibit interesting chiroptical phenomena outside of the Bragg reflection bands (photonic bandgaps), e.g., circular birefringence. For practical applications, BPI is of greater interest due to its much wider temperature range of existence (on the order of 10–100 kelvins, encompassing room temperature)^{29–31}.

Similar to photonic crystals formed from other soft matters (e.g., colloids), most naturally self-assembled BPLCs are polycrystalline. Usually, the sample is first heated to the isotropic liquid phase which

upon direct cooling produces polycrystals because the crystallites randomly nucleate, and the subsequent growth of the crystallites stops when meeting neighboring ones. The resulting small monocrystalline area ($\sim\mu\text{m}^2$) and high defect density significantly degrade their optical performance. To realize practical applications like optical beam processing and switching, larger single crystals (cm^2 or greater) are necessary for achieving sharp photonic band gaps, well-defined dispersion relations, and consistent optical properties over large spatial extent^{32–35}. Recently, growth of massive BPI single crystals, measuring up to cm^2 in area and 0.3 mm in thickness, on standard surface-treated substrates was achieved with a moving spatial temperature gradient, but the fabrication process is rather tedious and time-consuming [Fig. 1a]³⁵. Faster growth of BPLCs into mm^2 - to cm^2 -scale single crystals was also successfully demonstrated using special surface-alignment materials or nanostructures^{18,19,25}. Alternatively, studies have also shown that a high-frequency ($\sim\text{kHz}$) electric field^{36,37} or proper surface alignment²⁴ can effectively transform a polycrystalline BPLC sample into the so-called ‘monodomain’ crystals in a short time of a few seconds to a minute, with all the crystallites having the same crystalline axis (usually, $[110]_{\text{BCC}}$) along the applied field direction³⁸. However, the orthogonal crystalline axes of a monodomain crystal are randomly oriented if there is no surface alignment; on the other hand, although the orthogonal crystalline axes are approximately aligned in a BPLC that has surface alignment treatment, they still contain many grain boundaries and dislocations, resulting in suboptimal optical quality.

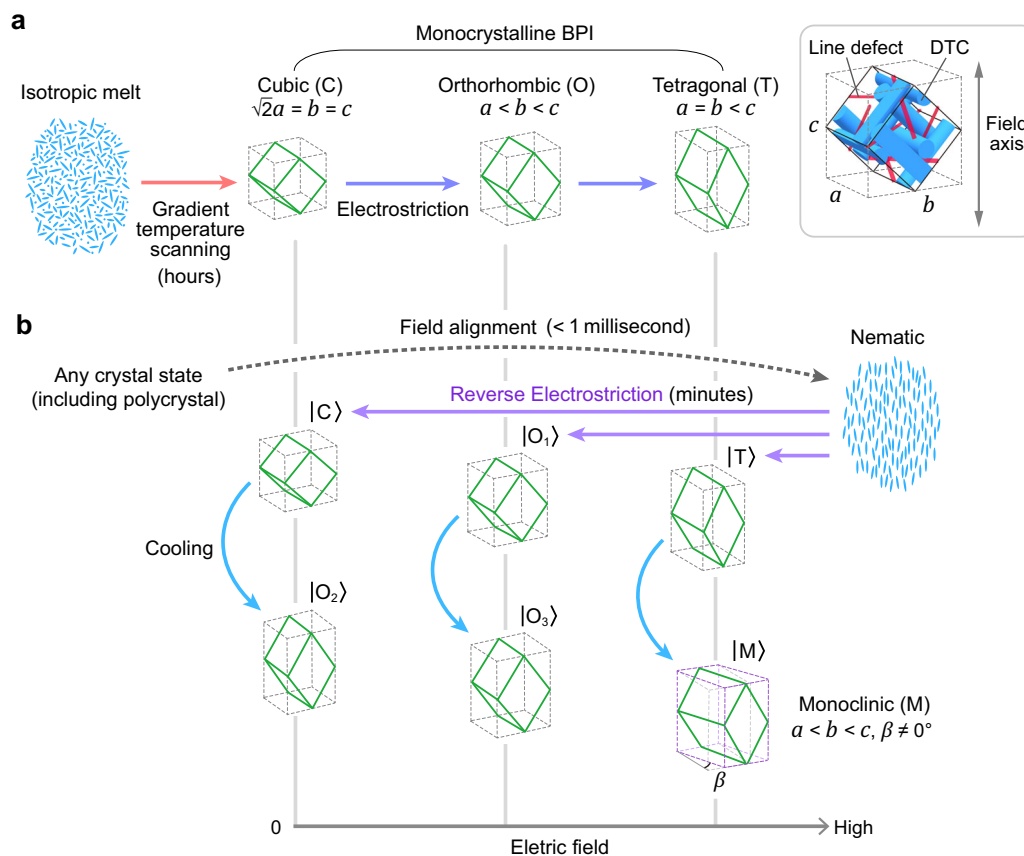


Fig. 1 | Reverse electrostriction directed assembly (REDA). **a** Conventional crystal-growth and electrostriction process, which takes several hours. **b** The REDA approach can achieve large-area monocrystalline BPLCs of various crystalline symmetries in minutes. Cooling a monocrystalline BPLC formed by REDA causes anisotropic lattice distortion and thereby transforms the crystal into different symmetries, including the never-before-seen monoclinic (M) symmetry. The capital letter in each $| \rangle$ denotes the crystal symmetry formed at a particular electric field

strength via REDA with or without additional cooling (C: cubic, O: orthorhombic, T: tetragonal, M: monoclinic). $|O_1\rangle$, $|O_2\rangle$, and $|O_3\rangle$ are orthorhombic states with different ratios of the lattice parameters. Inset at the upper right shows the crystal structure of a $[110]_{\text{BCC}}$ -oriented BPLC and associated lattice parameters a , b , and c (see Section *Lattice parameters and symmetries*). Skew angle β is the complementary angle to the angle formed between a and b axes (see Section *Monoclinic symmetry*).

Moreover, almost all existing crystal-growth techniques are limited to producing single crystals with simple, highly symmetric lattice structures: body-centered cubic in BPI and simple cubic in BPII. Lower crystal symmetries, such as tetragonal, orthorhombic, or monoclinic, could lead to more complex photonic band structures, offering more versatile control over light propagation and interaction within the crystal^{39–45}. This, in turn, would unlock a wider range of photonic functionalities and applications. To date, electrostriction is perhaps the only method to convert a cubic photonic crystal of BPLC to a lower symmetry structure post-growth^{46–48}. This process involves applying an electric field to rearrange the DTCs and line defects, deforming the lattice structure. In BPI, the induced symmetry transformation is oftentimes irreversible due to the nature of its defect structure (detailed in ref. 47.), making it nearly impossible to switch among different symmetries. Also, the entire process of growing a cm²-large single crystal of any symmetry usually takes hours due to the slow self-assembly of liquid crystal molecules [Fig. 1a].

In this work, we report a reverse electrostriction directed assembly (REDA) technique [Fig. 1b] that enables fabrication of monocrystalline BPLCs of large areal sizes and diverse symmetries in minutes. The technique is conceived following a detailed study on the complex evolution of BPLC lattices subjected to an applied field of varying strengths and at different ambient temperatures. By investigating different points in the phase space spanned by temperature, applied field, and liquid-crystal phases, we have gained new insights in the formation dynamics of various crystalline symmetries. In particular, we have discovered that starting from a highly ordered, homeotropic nematic phase (where the director axis of the DTCs and defect network is completely unwound and uniformly aligned) induced by a strong electric field near the BPI–BPII transition temperature and subsequent lowering of the applied field, one can efficiently direct the molecular assembly into monocrystalline BPLC of various symmetries (tetragonal, orthorhombic, cubic) in times much shorter than all other existing techniques. As will be presented in greater detail, this approach is a “reverse of the electrostriction process (that switches the BPI to the nematic phase)” and directs the molecular assembly to a targeted crystalline state—a single crystal of a specific symmetry—while avoiding some common issues in conventional crystallization processes; the high uniformly applied field from the very outset of the crystallization process quenches director-axis fluctuation, disallows random nucleation, and enforces uniformity over the entire crystal bulk during reassembly. Unlike existing approaches, here the crystallites nucleate directly with low symmetry and rapidly merge into a cm²-large single crystal of the desired symmetry within only 10–20 min. After the large single crystal is formed and the steady state is reached, varying the ambient temperature with a fixed applied field provides another means to reconfigure the crystals to have different lattice parameters (*a*, *b*, and *c* defined in the inset of Fig. 1) and their ratios, or even new crystal symmetry (e.g., monoclinic). These large-area photonic crystals with various lattice-parameter ratios and symmetries enable a wide range of photonic band structures and expand the potential for optical and photonic applications.

Results

Dynamic evolutions of BPLC from different initial states

Our study begins by examining the dynamic evolution of BPLC near the BPI–BPII transition temperature, which we discover to be the region where an applied electric field can be employed to direct the molecular self-assembly and crystalline-symmetry transformation to form large-area monocrystalline BPLCs with desired lattice structures.

A surface-treated cell of BPLC is placed on a temperature stage with a spatial temperature gradient maintained across the isotropic-to-ordered phase transition temperature. As a function of temperature variation from the hot to cooler regions, the isotropic (completely disordered) BPLC undergoes molecular self-assembly and nucleation

to two typical BPLC phases, BPII and then BPI as shown in Fig. 2a. In BPII, the nucleated crystallites easily merge into a large single crystal, whereas BPI crystallites tend to remain separated. This is mainly due to the fundamental difference between the defect networks in BPI and BPII³⁵, which affects the way to reduce the high free energy at grain boundaries. Specifically, in BPII, the line defects in a simple-cubic lattice intersect with each other, so the crystallites tend to align and merge with neighboring ones to form a continuous defect network and thus a single crystal (the global minimum of free energy). In BPI, however, even within a unit cell, the defects are well separated. Therefore, the crystallites tend to relax into their local energy minima and remain polycrystalline, rather than directly merge into a large single crystal; that said, BPI crystallites can still merge with neighboring ones, but it takes hours to days to form a millimeter-sized crystal, as shown in Fig. 2a. The self-assembly and merging process slows down as crystallites become larger, and a polycrystal of 100- μm -sized grains is obtained after several hours (see Supplementary Movie 1).

An interesting and important phenomenon is observed when a high applied field is applied to the sample to unwind all the doubly twisted cholesteric helices and randomly aligned director axis in the line defects in BPI and BPII, i.e., transition to the homeotropically aligned nematic phase which typically takes ~ 1 millisecond or less. When the high field is switched abruptly to a lower value, we observe that the BPI crystallites are nucleated. These crystallites are all oriented with their [110]_{BCC} axis (defined according to the BCC-coordinate convention) along the field axis and have identical in-plane crystalline axis due to surface alignment on the cell windows. Therefore, once neighboring crystallites meet, they can rapidly merge into larger ones, because they exhibit the same crystal orientation in the first place. A large single crystal of the size of the sample (centimeter in width) is formed within a few minutes, as shown in Fig. 2b [see Supplementary Movies 2 and 3]. This process of rapidly reducing the applied field strength to a low value is effectively reversing the electrostriction that takes the system to the nematic phase and guides the molecular assembly along a singular route to a specific crystalline orientation and structure, thereby forming of a single crystal of a defined symmetry.

It is important to note here that successful single-crystal formation occurs only at the high temperature end of BPI (near the BPI–BPII transition point). When the operating temperature is lower (away from the phase-transition point), the BPLC tends to settle into a polycrystal, as depicted in the lower part of the left panel in Fig. 2b. A plausible explanation is that, in general, the neighboring BPI crystallites do not have sufficient energy to overcome the energy barrier and merge into a larger crystal. However, at the high temperature end of BPI, the liquid crystal molecules have higher mobility for self-assembly to rapidly merge with other crystallites to grow larger (see Supplementary Note 1 for more details about temperature effect).

On the mesoscopic scale, formation of a large single BPI crystal also requires the DTCs to self-assemble with directionality in all three dimensions. In ref. 35., surface treatment of the cell windows defines the easy axis of DTC alignment in the cell plane, while the moving temperature gradient provides the direction of DTC self-assembly in the third dimension. Importantly, the moving temperature gradient needs to be slow enough to follow the DTC self-assembly³⁵. In the present study, we use surface-treated windows to define the in-plane easy axis (see Supplementary Note 1 for more details about alignment), but the directionality of crystal growth comes from the high initially applied field. The surface treatment and directional relaxation (by reversing the applied field to a lower value) work constructively as they both energetically favor the formation of [110]_{BCC}-oriented BPI crystals (see refs. 47,48.). We found that by reducing the high field to an intermediate level instead of turning it off completely, a single crystal of various non-cubic symmetries can be formed rapidly [Fig. 1]. The symmetry and lattice-parameter ratio of the single crystal are

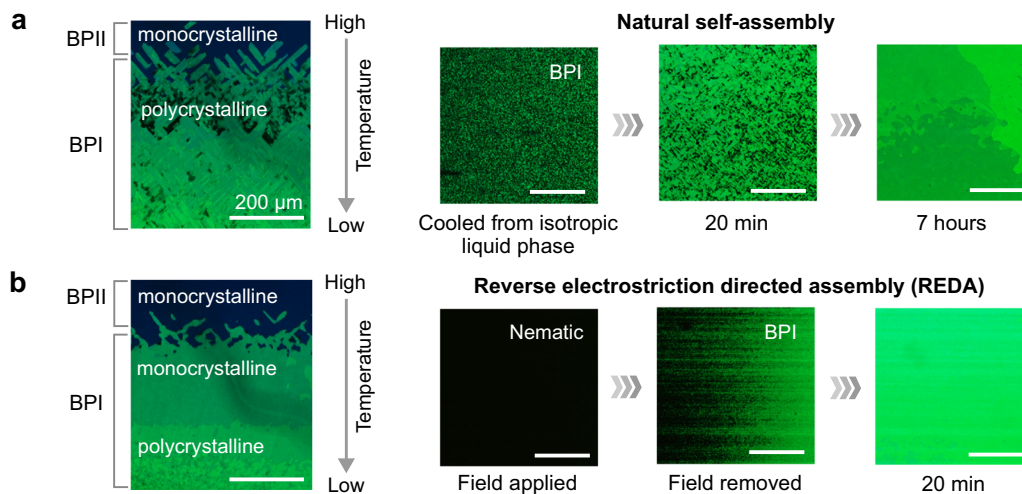


Fig. 2 | Natural self-assembly via cooling vs. reverse electrostriction directed assembly (REDA). **a, b** Polarized-optical-microscope images of a BPLC with temperature gradient of $-0.8\text{ }^\circ\text{C}/\text{mm}$ closed to the BPI–BPII phase-transition point of $31.7\text{ }^\circ\text{C}$ (left) and the dynamics of crystal growth (right): **a** crystal growth via direct cooling from the isotropic liquid phase (see Supplementary Movie 1 for video),

b crystal growth via relaxation from a highly ordered state (i.e., the field-induced nematic phase) upon field removal (see Supplementary Movies 2 and 3 for videos). REDA enables the formation of a BPI single crystal near the BPI–BPII phase-transition point. Temperatures are maintained at $-0.1\text{ }^\circ\text{C}$ below the phase-transition point. Surface-alignment films were rubbed from left to right.

determined by the intermediate field strength (see Section *Lattice parameters and symmetries*).

The discovery of a temperature range where one can employ an applied field to first bring the system to a highly ordered state and then direct the system to assemble into large monocrystalline BPLC with diverse symmetries in a much shorter time than conventional crystallization motivates us to conduct more quantitative systematic studies. The ensuing sections provide detailed accounts of exemplary results, analyses, new discoveries, and in-depth discussions.

Reverse electrostriction directed assembly

Fig. 3a, b shows the entire process of reverse electrostriction directed assembly (REDA) from the high-field application to directed assembly by a lower directing field, temperature tuning at a constant bias AC field (with the same magnitude as the directing field), and finally the field removal.

The starting point of REDA is a BPLC maintained at the temperature near the BPI–BPII transition point and on which a high electric field (E_H) of $-12.3\text{ V}/\mu\text{m}$ is applied to unwind all the DTCs and align the liquid crystal molecules to the homeotropic nematic state, within a millisecond. Here a dark image is observed under a cross-polarized microscope because the optic axis of the field-induced nematic liquid crystal is parallel to the viewing direction [Fig. 3b]. The high electric field is then rapidly switched to a lower field, in about 1 or 2 ms, to avoid undesirable effects caused by dielectric heating or electrohydrodynamic instabilities, which can occur when the high field is applied for a longer duration. Upon switching to the (lower) directing field (E_D), BPI crystallites of similar lattice orientations (determined by the field axis and surface-alignment direction) nucleate, neighboring crystallites then rapidly merge to form larger ones, and finally a large single crystal of a particular symmetry is grown in several minutes [Fig. 3b and Supplementary Movie 4].

As shown in Fig. 3c, the Bragg-reflection wavelength of the nucleated crystallites undergoes a rapid initial drop (blueshift), followed by a gradual stabilization to a steady-state value. This behavior indicates that crystallites nucleate directly with a low-symmetry structure of fairly large lattice parameter along the field axis and subsequently undergo lattice refinement to achieve the final desired structure. The time required to reach the steady state increases with increasing directing field strength (E_D): from $\sim 50\text{ s}$ for $E_D = 0\text{ V}/\mu\text{m}$ to $\sim 200\text{ s}$ for $E_D = 4\text{ V}/\mu\text{m}$. The final Bragg wavelength also depends on E_D ,

with higher fields resulting in longer wavelengths. As will be discussed in Section *Lattice parameters and symmetries*, careful analysis of the corresponding crystal-diffraction patterns (Kossel diagrams, e.g., Fig. 3b inset) reveals cubic symmetry for $E_D = 0\text{ V}/\mu\text{m}$, orthorhombic symmetry for E_D between 0 and $-3\text{ V}/\mu\text{m}$, and tetragonal symmetry for E_D between -3 and $5.6\text{ V}/\mu\text{m}$.

It is interesting and instructive to compare Fig. 3c with the spectral shift towards shorter wavelengths (obtained with reversing the electrostriction) and Fig. 3d obtained with conventional electrostriction (applying increasing field strength). In conventional electrostriction^{46–48}, the applied field reorients BPLC lattices such that the $[110]_{\text{BCC}}$ axis aligns with the field axis^{36,38}. Meanwhile, their lattices are stretched along the field axis, transforming from the cubic symmetry, through orthorhombic, to tetragonal symmetry, and the spectral shift of the Bragg reflection towards longer wavelengths [Fig. 3d]⁴⁷. These observations suggest that the applied field dictates both the preferred crystal orientation and symmetry of BPI, explaining the effectiveness of REDA in producing single crystals. In REDA, the field directs the BPI crystallites to nucleate with a specific orientation (the $[110]_{\text{BCC}}$ axis parallel to the field axis) and symmetry (cubic, orthorhombic, or tetragonal depending on the directing field strength). Notably, unlike conventional electrostriction which has been extensively studied through simulations^{49,50}, the reverse electrostriction has never been predicted by any numerical studies.

Furthermore, after the crystal symmetry has settled to a steady state, temperature tuning at the constant applied field allows us to alter the crystal's lattice parameters (defined in the next section). The cooling process (by $-1\text{ }^\circ\text{C}$ at a rate of $0.1\text{ }^\circ\text{C}/\text{min}$) allows tuning the ratio among the three principal lattice parameters for a given symmetry; it also enables transforming the crystal to a new symmetry, such as the monoclinic symmetry that, to our knowledge, has never been discovered before in blue phases (see Section *Monoclinic symmetry*). We have also observed that operating at a lower temperature makes the lattice structure even more stable, owing to the increase in the liquid crystal viscosity and free-energy barrier. These low-symmetry single crystals are stable even after switching off the applied field.

Lattice parameters and symmetries

To quantify the crystalline structure of a BPLC formed by REDA, lattice parameters a , b , and c are defined as follows. As illustrated in the upper left inset in Fig. 1, the lattice structure of a $[110]_{\text{BCC}}$ -oriented BPLC can

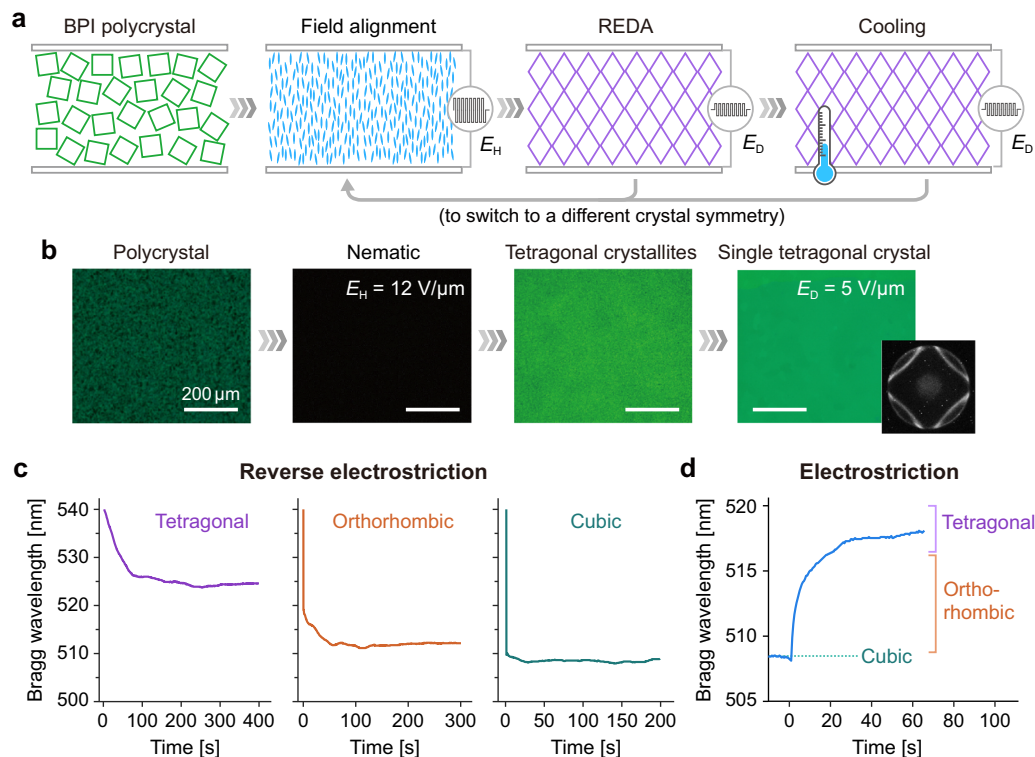


Fig. 3 | Reverse electrostriction vs. electrostriction. a, b (a) Schematic and (b) optical micrographs showing each state of a BPLC in the process of reverse electrostriction and cooling to form a single crystal of target symmetry: initial polycrystal → electrically induced nematic at field strength of $E_H = 12 \text{ V}/\mu\text{m}$ → nucleated crystallites after reducing the applied field strength to $E_D = 5 \text{ V}/\mu\text{m}$ → single tetragonal crystal formed through natural merging of neighboring crystallites (see Supplementary Movie 4 for video). Temperature is maintained at 31.6°C , -0.1°C

below the BPI–BPII phase-transition point. Surface-alignment (rubbing) direction is from left to right. **c** Time-resolved Bragg-reflection wavelength showing different dynamics of reverse electrostriction. The Bragg reflection band rapidly blue-shifts and then settles to a spectral location depending on the directing field strength (E_D). The field strengths are 4.0 , 2.6 , and $0.0 \text{ V}/\mu\text{m}$ for the tetragonal, orthorhombic, and cubic symmetries, respectively. **d** Conventional electrostriction, an electric field at $3.2 \text{ V}/\mu\text{m}$ is applied for 60 s to induce lattice deformation.

be described using a set of basis vectors **a**, **b**, and **c**. The corresponding lattice parameters are the magnitudes of these vectors: $a = |\mathbf{a}|$, $b = |\mathbf{b}|$, and $c = |\mathbf{c}|$. The **c** vector aligns with the $[110]_{\text{BCC}}$ axis, typically parallel to the applied field, cell normal, and the optical axis of the imaging system. The **a** and **b** vectors, perpendicular to the applied field, lie along the $[001]_{\text{BCC}}$ and $[-110]_{\text{BCC}}$ axes, respectively. We have developed a fitting algorithm capable of extracting these lattice parameters (*a*, *b*, and *c*) from a measured Kossel diagram, an orthogonal projection of the crystal's far-field diffraction onto an image plane (details on the experimental setup and fitting algorithm can be found in Supplementary Note 2)⁵¹. This approach provides valuable and new insights into the crystal structures.

First, without any applied fields, BPI crystals obtained by cooling directly from the isotropic melt are commonly assumed to exhibit a BCC symmetry. However, through careful Kossel analysis, we find that the BPI crystal begins to depart from the cubic symmetry upon cooling from the BPII–BPI transition point as shown in Fig. 4a. Specifically, just below the transition temperature (32.1°C), the lattice parameters of $c = b = \sqrt{2}a$ is characteristic of a cubic BPI crystal oriented with its $[110]_{\text{BCC}}$ axis along the view axis. As the temperature drops, *c* gradually increases, while *b* and *a* decrease. The fact that $c \neq b \neq \sqrt{2}a$ clearly indicates that a spontaneous transformation to an orthorhombic symmetry has occurred. The observed anisotropy of the lattice deformation during cooling is attributed to the disparity in boundary conditions and lattice dimensions along different axes. The longitudinal lattice boundary interacts with a surface-alignment layer on the glass window, and the thickness is only $12 \mu\text{m}$ (equivalent to $30\text{--}40$ unit cells). By contrast, the lateral dimensions of the crystal and constituent DTCs reach centimeters, significantly larger than the longitudinal dimension. The lateral crystal deformation due to cooling

is countered by the elastic restoring force exerted by a vast number of unit cells. Notably, the anisotropy of the cooling-induced lattice deformation has never been observed experimentally before, nor numerically. Numerical simulations of such behavior require significant computational power due to the large system size (at least $10^4 \times 10^4 \times 30$ unit cells) needed to capture the field-induced dynamics of a BPI lattice^{49,50,52,53}.

In stark contrast to Fig. 4a, b shows that the BPI crystals induced by reverse electrostriction with zero directing field ($E_D = 0 \text{ V}/\mu\text{m}$) exhibit nearly constant lattice parameter ratios across temperatures, preserving the cubic symmetry. The calculated *c*:*a* and *b*:*a* ratios are all ~ 1.4 , consistent with the expected $\sqrt{2}$ ratio of a BCC lattice. Interestingly, despite similar ratios, the actual values of *a*, *b*, and *c* increase with decreasing temperature. This increase likely originates from a reduced twisting power of the chiral agent in the BPLC mixture at lower temperatures.

As described earlier, besides the cubic symmetry ($E_D = 0$), orthorhombic ($E_D \lesssim 3 \text{ V}/\mu\text{m}$) and tetragonal ($E_D \approx 3\text{--}5.6 \text{ V}/\mu\text{m}$) single crystals can also be formed by REDA. Figure 4c shows the dependence of lattice parameters on the directing field strength. While *b* and *c* gradually deviate from each other with increasing E_D , *a* and *b* become closer and converge to almost the same value at $E_D \approx 3 \text{ V}/\mu\text{m}$, where a transition from orthorhombic to tetragonal symmetry occurs [circles and dashed lines in Fig. 4c]. Upon cooling, anisotropic lattice deformation also occurs in all the low-symmetry single crystals formed at different E_D [diamonds and solid lines in Fig. 4c]. For $E_D \lesssim 3 \text{ V}/\mu\text{m}$ and $E_D \gtrsim 4 \text{ V}/\mu\text{m}$, the crystal symmetry (orthorhombic or tetragonal) remains the same, but the lattice parameter ratio (*a*:*b*:*c*) has changed; in general, *c* is elongated, while both *a* and *b* contracted (see Fig. 4d for the Kossel diagrams and optical micrographs corresponding to

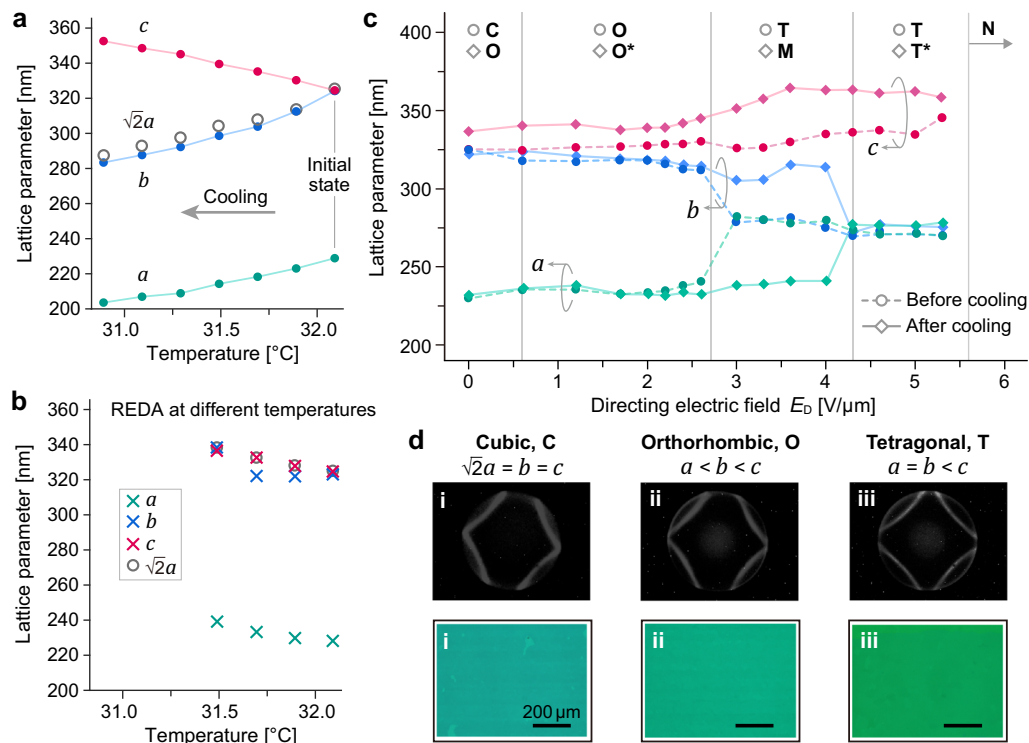


Fig. 4 | Cooling-induced anisotropic lattice deformation. **a**, **b** Temperature-dependent lattice parameters (a , b , and c) of BPLC single crystals formed via **(a)** direct cooling from 32.1 °C (initial state prepared by REDA) or **(b)** REDA at the designated temperature. Panel **a** shows that the crystal transforms from cubic ($b = c$) to orthorhombic ($b < c$) symmetry upon cooling. Panel **b** shows that REDA with zero directing field in the relaxation stage forms a cubic crystal ($a\sqrt{2} = b = c$), regardless of temperature. **c** Lattice parameters of BPLC crystals formed at various applied directing field strengths (E_D) of REDA with or without additional cooling (by

-1 °C), showing that the cooling transforms a crystal to one with either the same symmetry but a different lattice-parameter ratio or a different symmetry. **C**: cubic, **O**: orthorhombic, **T**: tetragonal, **M**: monoclinic, **N**: homeotropic nematic, *****: same symmetry but different lattice-parameter ratio. **d** Kossel diagrams and optical micrographs of BPLC single crystals with different symmetries formed via REDA. Field strengths are 4.0, 2.6, and 0.0 V/ μm for the tetragonal, orthorhombic, and cubic symmetries, respectively. Surface-alignment directions are all from left to right.

different E_D). For crystals formed between $E_D \approx 3$ and 4 V/ μm , the tetragonal crystal has transformed into a new symmetry—monoclinic (see the next section for detailed discussion).

Monoclinic symmetry

For directing field strengths E_D between -3 and -4 V/ μm , we observe dramatic changes in both the Kossel diagram and crystal texture upon cooling. As depicted in Fig. 4d, the Kossel diagram of a tetragonal crystal formed at the high temperature end of BPI range shows four arcs (part of Kossel rings in the field of view) arranged in a four-fold symmetry. Figure 5a shows that more arcs appear in the diagram upon cooling. Meanwhile, the crystal texture turns from uniform to cross-hatched [Fig. 4d(iii) photo vs. Fig. 5b]. Both are signs of crystal twinning. (It is important to distinguish the twinning observed here, which originates from cooling of a tetragonal single crystal, from the twinning induced by martensitic transformation from a simple-cubic lattice of BPII to a BCC lattice of BPI reported elsewhere^{48,54–57}.) The tetragonal single crystal has fractured into many twinned crystals (i.e., pairs of single crystals with different orientations), evident as striations (alternating bright and dark bands) observed under a polarizing optical microscope [Fig. 5b]. In Fig. 5a(i), the six-arc-like Kossel pattern come from, in fact, two sets of four Kossel rings [Fig. 5a(ii) and 5a(iii)], and two of the four arcs in one set are spatially overlapped with two of the four arcs in the other set (rings \odot and \ominus).

Let's first focus on one set of the Kossel rings, corresponding to one of the twins [Fig. 5a(ii) or 5a(iii)]. One may notice that the four-arc pattern of either twin shows two-fold symmetry but is distorted from that of a typical orthorhombic crystal [cf. Fig. 4d(ii)]. This indicates that the lattice is not rectangular in the lateral dimensions. We retrieve the

lateral crystallographic axes (the a and b axes) from the Kossel diagram and find that the angle between the two axes is no longer 90°, as schematically depicted in Fig. 5c (note that the angle is not to scale for schematic purpose). Thus, a skew angle β is defined as the complementary angle to the angle formed between the a and b axes. Having a nonzero skew angle is characteristic of a monoclinic crystal structure, which has not been observed in BPLCs before. The formation of the twinned monoclinic crystal can be attributed to the inability of a single tetragonal crystal to sustain the anisotropic lattice deformation during cooling; that is, the strong shear elastic force causes the single tetragonal crystal to break into pairs of monoclinic crystals. Comparing the Kossel diagram of the parent tetragonal crystal to that of the monoclinic twinned crystals [Fig. 4d(iii) vs. 5a(i)], the upper left and lower right rings of the parent [Fig. 4d(iii)] break into rings \odot , \ominus and rings \ominus , \odot of the twins, respectively [Fig. 5a(i)]. As further illustrated in Fig. 5c, the twinned crystals have skew angles of equal magnitude but opposite signs.

Quantitative measurements of the E_D -dependent lattice parameters and skew angle are shown in Figs. 4c and 5d. Figure 4c reveals that, upon transition from the tetragonal state, $a \approx b \approx 280$ nm, into the monoclinic state, a decreases to ~ 240 nm, while b increases to ~ 320 nm. Although the values of a and b in the monoclinic state ($3 \text{ V}/\mu\text{m} \lesssim E_D \lesssim 4 \text{ V}/\mu\text{m}$) are close to those measured in the orthorhombic state ($E_D \lesssim 3 \text{ V}/\mu\text{m}$), the skew angle β clearly distinguishes the monoclinic crystal from orthorhombic (and tetragonal) crystals. Figure 5d shows that, below $-3 \text{ V}/\mu\text{m}$ and above $-4 \text{ V}/\mu\text{m}$, the skew angle $\beta = 0^\circ$ as the BPLC is either in the monocrystalline orthorhombic state or in the monocrystalline tetragonal state. Above $-3 \text{ V}/\mu\text{m}$, β first rises with increasing E_D to 2.5° at $3.3 \text{ V}/\mu\text{m}$ and then drops to zero at

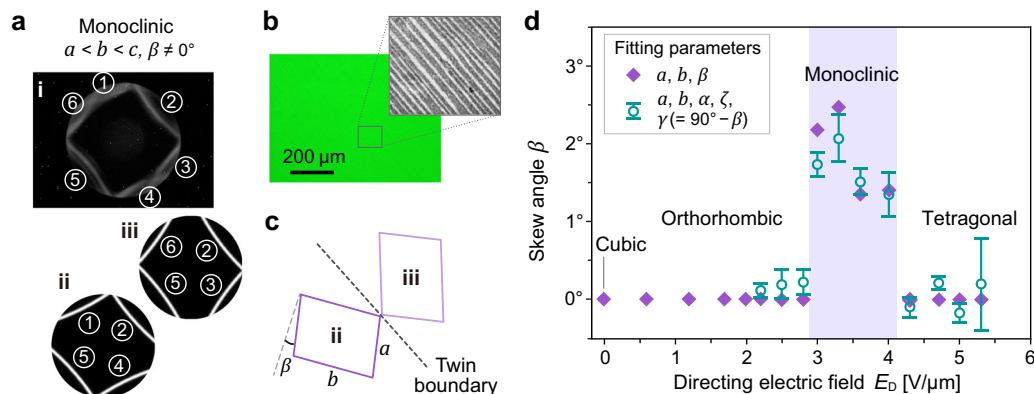


Fig. 5 | Twinned crystal with monoclinic symmetry. A twinned monoclinic crystal is formed by cooling a tetragonal single crystal (from 31.6 °C to 30.7 °C) with field maintained at 3.6 V/μm. **a** Kossel diffraction pattern (i) showing a total of six rings (or, arcs due to limited field of view), which can be decomposed into two sets of Kossel rings (ii, iii). The two sets share rings ② and ⑤, and each set represents one of the twins. Both patterns (ii, iii) appear as a sheared version of the Kossel pattern observed in an orthorhombic crystal (cf. Fig. 4d(ii)), suggesting the presence of monoclinic crystals. **b** Optical micrographs of the twinned monoclinic crystal. Contrast and brightness of the grayscale micrograph in the inset are adjusted to show the striated texture due to crystal twinning. Surface-

alignment (rubbing) direction is from left to right (a, b). **c** Schematic depicting the unit-cell orientations of monoclinic twins on opposite sides of twin boundary (dashed line), and definition of skew angle β . **d** Skew angle β of monoclinic BPLC as a function of the directing field strength (E_D) during REDA. At E_D between -3 and -4 V/μm², monoclinic crystals ($\beta \neq 0$) can be formed through direct cooling from a tetragonal single crystal. Purple diamonds represent fits with a , b , and β as free parameters. Green open circles represent a more rigorous analysis where the angles between all three basis vectors (a , b , and c) are treated as independent fitting parameters, α , ζ , γ ($\gamma = 90^\circ - \beta$) (details in Supplementary Note 2). Error bars represent the standard deviation.

-4 V/μm. To exclude the possibility of other crystal systems (such as triclinic), we perform a more rigorous fitting analysis. This approach treats the angles between all three basis vectors (a , b , and c) as independent fitting parameters. Details regarding the fitting process can be found in Supplementary Note 2. The resulting fitted values (green squares with error bars in Fig. 5d) are in good agreement with our initial characterization of the crystals. It is worth noting again that these twinned monoclinic crystals are stable after field removal.

Large-area photonic crystals covering full visible spectrum

The REDA technique is employed to fabricate monocrystalline BPLCs with different Bragg reflection bands across the visible spectrum. Such spectral tuning of the Bragg reflection is achieved by varying the material chirality (i.e., changing the concentration of the chiral dopant). Initially, all three BPLC samples exhibit polycrystalline structures, as shown in Fig. 6a. Subsequently, the application of REDA results in the rapid formation of large-area monocrystalline BPLC as depicted in Fig. 6b; each sample has an approximate size of ~1 cm². The observed sharp reflection bands with narrow bandwidth shown in Fig. 6c serve as clear indicator of the high-quality crystal structure achieved. Importantly, this technique circumvents limitations on sample size, as the resulting monocrystalline BPLC dimensions are determined by the size of the uniform electric field area. Using different directing field strengths (E_D) in REDA allows for further control over the photonic bandgap by transforming the crystalline symmetry and the corresponding reflection spectra, as shown in Fig. 6d. These reflection bands do not shift and remain narrow after field removal, confirming the high stability of the single crystals.

Discussion

Our systematic study of BPLC lattice transformation under an applied electric field has revealed new findings and valuable insights into the dynamic evolution and reconfiguration of BPLCs into diverse photonic crystal structures. The conventional approaches of temperature-induced crystal growth with post-crystallization field treatments suffer from long processing time (hours), high defect density, and/or limited crystal symmetries. In great contrast, the reverse electrostriction approach (REDA), starting from a highly ordered phase with unidirectionally aligned director axes, allows for rapid formation of large

single crystals with cubic, orthorhombic, or tetragonal symmetry, in 10–20 min. Through further temperature tuning (while maintaining the applied field used in REDA), we have unveiled two intriguing phenomena: anisotropic lattice deformation (which provides another means to control over lattice parameters) and the emergence of previously unseen monoclinic crystal structures. Our technique successfully realizes stable, large-area, monocrystalline BPLCs with diverse crystalline symmetries and photonic bandgaps spanning the entire visible spectrum, opening the door to a wider range of optical and photonic applications.

This expanded diversity of monocrystalline lattice structures unlocks exciting potential for soft matter-based photonic crystals. The capability of tailoring a BPLC's lattice structure allows one to control the Bragg reflections and dispersion properties. Together with the intrinsic nonlinear optical properties of liquid crystals, it is possible to achieve ultrafast pulse compression, modulation, and optical switching^{58,59}. Moreover, BPLC's chirality enables manipulation of circularly polarized light via circular dichroism and optical activity^{60,61}, offering promising possibilities in chiral sensors, lasers, and quantum optics.

Methods

Materials

In Figs. 2–5, and S1, the BPLCs with green reflection consist of 55.5 wt% HTW114200-050, 36.5 wt% R811 (with a helical twisting power of -11 μm⁻¹), 4.0 wt% RM257 (all from HCCH), and 4.0 wt% 2-ethylhexyl acrylate (EHA, from Sigma-Aldrich). The mixture showed a phase sequence of ISO(-35.6 °C)–BPII(-31.7 °C)–BPI(-27.2 °C)–N* (ISO: isotropic liquid phase, N*: cholesteric phase). In Fig. 6, the BPLC with orange reflection consists of 58.0 wt% HTW114200-050, 34.0 wt% R811, 4.0 wt% RM257, and 4.0 wt% EHA, showing a phase sequence of ISO(-41.7 °C)–BPII(-41.4 °C)–BPI(-36.0 °C)–N*. The BPLC with blue reflection consists of 48.8 wt% HTW114200-050, 43.2 wt% R811, 4.0 wt% RM257, and 4.0 wt% EHA, showing a BPII–BPI phase transition at -25 °C and the transition temperature to N* below 20.0 °C.

Cell assembly

BPLCs are enclosed in glass cells comprising two rectangular indium-tin-oxide (ITO) glass windows separated by polymer microspheres of

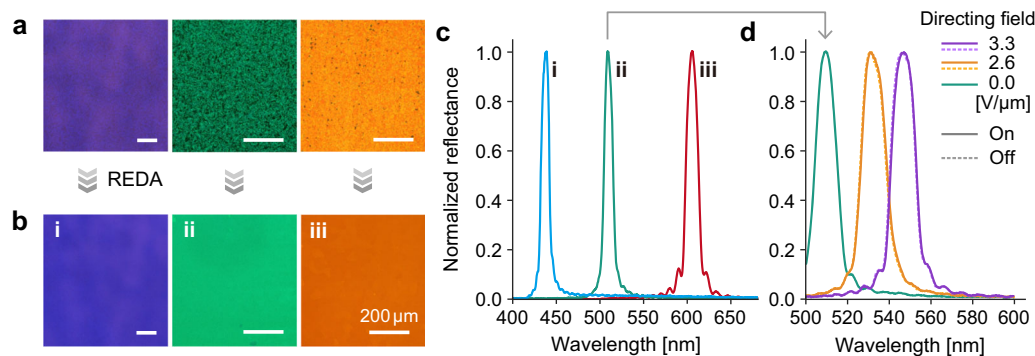


Fig. 6 | Diverse-symmetric photonic crystals across the visible spectrum.

Changing the intrinsic chirality by varying the material composition enables tuning of the Bragg reflection band across the visible spectrum. **a** Optical micrographs of polycrystalline BPLCs. **b, c** (b) Optical micrographs and (c) reflection spectra showing that, regardless of the material chirality, reverse electrostriction directed assembly (REDA) can be utilized to generate a large single crystal with sharp Bragg

reflection band. Temperatures are 24.9, 31.6, and 37.9 °C for BPLCs with blue, green, and orange reflections, respectively. Surface-alignment (rubbing) direction is from left to right. **d** Reflection spectra showing that single crystals of different lattice structures can be formed by varying the directing field strength (E_D) of REDA. After field removal, their reflection bands do not shift and remain narrow, confirming the high stability of these single crystals.

12 μm in diameter. Before cell assembly, the ITO side of each glass window is treated with a surface-alignment layer for orienting the liquid crystal molecules at the interface. Two methods are employed in this study. For samples used in Figs. 2, 3, 4c, d, 5, 6, and S3–S5, the windows are coated with a thin (~100 nm) film of polyvinyl alcohol. This film is then rubbed with a velvet-covered drum to create an in-plane easy axis that guides the liquid crystal molecules to align along the rubbing direction. For samples used in Figs. 4a, b and S1, the windows are coated with a thin layer of diazo dye brilliant yellow and then exposed to a linearly polarized, continuous-wave laser beam at a wavelength of 457 nm and an intensity of 110 mW/cm². The laser light aligns the dye molecules perpendicular to its polarization. The aligned dye guides the liquid crystal molecules to adopt a similar orientation at the interface. To assemble the cell, polymer microspheres are deposited near the edges of one window (on the ITO side). Then, we cover this window with another one, positioning its ITO side inward. The two glass windows are shifted by a few millimeters to facilitate wiring out the electrodes, and the edges of the cell without exposed electrodes are sealed with epoxy adhesive. Next, BPLCs are heated to the isotropic liquid phase and introduced into the glass cells through capillary action. Finally, the entire cell is sealed using epoxy adhesive for complete closure. The ITO electrodes of the BPLC cells are extended using copper tapes for connection to the voltage source.

Optical characterization

The optical micrographs are captured using a polarized optical microscope Eclipse LV100 POL (from Nikon) equipped with a camera DS-Fi1 (from Nikon). The white light source is a halogen light bulb (64610 HLX, from Osram). The reflection spectra are obtained by replacing the camera with a spectrometer (USB4000+, from Ocean Optics). To capture Kossel diagrams, we use the same polarized optical microscope with a Bertrand lens in the optical path and a 5-nm bandpass filter at 405 nm (see Supplementary Note 2 for more details).

Data availability

Data are available at <https://doi.org/10.5281/zenodo.12792108>⁶².

Code availability

Codes are available at <https://doi.org/10.5281/zenodo.12792301>⁶³.

References

- Lin, S. Y. et al. A three-dimensional photonic crystal operating at infrared wavelengths. *Nature* **394**, 251–253 (1998).

- Noda, S., Tomoda, K., Yamamoto, N. & Chutinan, A. Full three-dimensional photonic bandgap crystals at near-infrared wavelengths. *Science* **289**, 604–606 (2000).
- Campbell, M., Sharp, D. N., Harrison, M. T., Denning, R. G. & Turberfield, A. J. Fabrication of photonic crystals for the visible spectrum by holographic lithography. *Nature* **404**, 53–56 (2000).
- Aoki, K. et al. Microassembly of semiconductor three-dimensional photonic crystals. *Nat. Mater.* **2**, 117–121 (2003).
- Qi, M. et al. A three-dimensional optical photonic crystal with designed point defects. *Nature* **429**, 538–542 (2004).
- King, J. S. et al. Infiltration and inversion of holographically defined polymer photonic crystal templates by atomic layer deposition. *Adv. Mater.* **18**, 1561–1565 (2006).
- Xia, Y., Gates, B., Yin, Y. & Lu, Y. Monodispersed colloidal spheres: old materials with new applications. *Adv. Mater.* **12**, 693–713 (2000).
- Ozin, G. A. & Yang, S. M. The race for the photonic chip: colloidal crystal assembly in silicon wafers. *Adv. Funct. Mater.* **11**, 95–104 (2001).
- Vlasov, Y. A., Bo, X.-Z., Sturm, J. C. & Norris, D. J. On-chip natural assembly of silicon photonic bandgap crystals. *Nature* **414**, 289–293 (2001).
- He, M. et al. Colloidal diamond. *Nature* **585**, 524–529 (2020).
- Wright, D. C. & Mermin, N. D. Crystalline liquids: the blue phases. *Rev. Mod. Phys.* **61**, 385 (1989).
- Rey, A. D. Liquid crystal models of biological materials and processes. *Soft Matter* **6**, 3402–3429 (2010).
- Yan, J. et al. Extended Kerr effect of polymer-stabilized blue-phase liquid crystals. *Appl. Phys. Lett.* **96**, 071105 (2010).
- Chen, Y.-H., Wang, C.-T., Yu, C.-P. & Lin, T.-H. Polarization independent Fabry-Pérot filter based on polymer-stabilized blue phase liquid crystals with fast response time. *Opt. Express* **19**, 25441–25446 (2011).
- Lowe, A. M. & Abbott, N. L. Liquid crystalline materials for biological applications. *Chem. Mater.* **24**, 746–758 (2012).
- Yoshida, H. et al. Secondary electro-optic effect in liquid crystalline cholesteric blue phases. *Opt. Mater. Express* **4**, 960–968 (2014).
- Lee, M.-J., Chang, C.-H. & Lee, W. Label-free protein sensing by employing blue phase liquid crystal. *Biomed. Opt. Express* **8**, 1712–1720 (2017).
- Martínez-González, J. A. et al. Directed self-assembly of liquid crystalline blue-phases into ideal single-crystals. *Nat. Commun.* **8**, 15854 (2017).
- Oton, E., Netter, E., Nakano, T., D.-Katayama, Y. & Inoue, F. Monodomain blue phase liquid crystal layers for phase modulation. *Sci. Rep.* **7**, 44575 (2017).

20. Wang, M. et al. Bias-polarity dependent bidirectional modulation of photonic bandgap in a nanoengineered 3D blue phase polymer scaffold for tunable laser application. *Adv. Opt. Mater.* **6**, 1800409 (2018).
21. Khoo, I. C. Cholesteric and blue-phase liquid photonic crystals for nonlinear optics and ultrafast laser pulse modulations. *Liq. Cryst. Rev.* **6**, 53–77 (2018).
22. Yang, J. et al. Liquid crystalline blue phase materials with three-dimensional nanostructures. *J. Mater. Chem. C*, **7**, 13352–13366 (2019).
23. Yang, J. et al. Fabrication and photonic applications of large-domain blue phase films. *J. Mater. Chem. C*, **7**, 9460–9466 (2019).
24. Manda, R. et al. Electrically tunable photonic band gap structure in monodomain blue-phase liquid crystals. *NPG Asia Mater.* **12**, 42 (2020).
25. Otón, E. et al. Orientation control of ideal blue phase photonic crystals. *Sci. Rep.* **10**, 10148 (2020).
26. Yang, Y., Wang, L., Yang, H. & Li, Q. 3D chiral photonic nanostructures based on blue-phase liquid crystals. *Small Sci.* **1**, 2100007 (2021).
27. Bisoyi, H. K. & Li, Q. Liquid crystals: versatile self-organized smart soft materials. *Chem. Rev.* **122**, 4887–4926 (2022).
28. Bagchi, K., Emeršič, T., Martínez-González, J. A., de Pablo, J. J. & Nealey, P. F. Functional soft materials from blue phase liquid crystals. *Sci. Adv.* **9**, eadh9393 (2023).
29. Coles, H. J. & Pivnenko, M. N. Liquid crystal ‘blue phases’ with a wide temperature range. *Nature* **436**, 997–1000 (2005).
30. Castles, F. et al. Blue-phase templated fabrication of three-dimensional nanostructures for photonic applications. *Nat. Mater.* **11**, 599–603 (2012).
31. Hu, W. et al. Ultrastable liquid crystalline blue phase from molecular synergistic self-assembly. *Nat. Commun.* **12**, 1440 (2021).
32. Blanco, A. et al. Large-scale synthesis of a silicon photonic crystal with a complete three-dimensional bandgap near 1.5 micrometres. *Nature* **405**, 437–440 (2000).
33. Deubel, M. et al. Direct laser writing of three-dimensional photonic-crystal templates for telecommunications. *Nat. Mater.* **3**, 444–447 (2004).
34. Zhou, J. et al. Large-area crack-free single-crystal photonic crystals via combined effects of polymerization-assisted assembly and flexible substrate. *NPG Asia Mater.* **4**, e21 (2012).
35. Chen, C.-W. et al. Large three-dimensional photonic crystals based on monocrystalline liquid crystal blue phases. *Nat. Commun.* **8**, 727 (2017).
36. Chen, Y. & Wu, S.-T. Electric field-induced monodomain blue phase liquid crystals. *Appl. Phys. Lett.* **102**, 171110 (2013).
37. Cho, S., Takahashi, M., Fukuda, J.-i., Yoshida, H. & Ozaki, M. Directed self-assembly of soft 3D photonic crystals for holograms with omnidirectional circular-polarization selectivity. *Commun. Mater.* **2**, 39 (2021).
38. Pierański, P., Cladis, P. E., Garel, T. & Barbet-Massin, R. Orientation of crystals of blue phases by electric fields. *J. Phys. Fr.* **47**, 139–143 (1986).
39. Anderson, C. M. & Giapis, K. P. Symmetry reduction in group 4mm photonic crystals. *Phys. Rev. B* **56**, 7313 (1997).
40. Schilling, J. et al. Three-dimensional macroporous silicon photonic crystal with large photonic band gap. *Appl. Phys. Lett.* **86**, 011101 (2004).
41. Poole, Z. et al. Holographic fabrication of three-dimensional orthorhombic and tetragonal photonic crystal templates using a diffractive optical element. *Appl. Phys. Lett.* **91**, 251101 (2007).
42. Khanikaev, A. B. & Steel, M. J. Low-symmetry magnetic photonic crystals for nonreciprocal and unidirectional devices. *Opt. Express* **17**, 5265–5272 (2009).
43. Hosein, I. D., Lee, S. H. & Liddell, C. M. Dimer-based three-dimensional photonic crystals. *Adv. Funct. Mater.* **20**, 3085–3091 (2010).
44. Kontogeorgos, A. et al. Inducing symmetry breaking in nanostructures: anisotropic stretch-tuning photonic crystals. *Phys. Rev. Lett.* **105**, 233909 (2010).
45. Yannopoulos, V. One-way photonic band gaps and optical isolation with three-dimensional photonic crystals of low symmetry. *Phys. Rev. A* **88**, 043837 (2013).
46. Heppke, G., Jérôme, B., Kitzerow, H.-S. & Pieranski, P. Electrostriction of the cholesteric blue phases BPI and BPII in mixtures with positive dielectric anisotropy. *J. Phys. Fr.* **50**, 2991–2998 (1989).
47. Guo, D.-Y. et al. Reconfiguration of three-dimensional liquid-crystalline photonic crystals by electrostriction. *Nat. Mater.* **19**, 94–101 (2020).
48. Zhang, Y. et al. Three-dimensional lattice deformation of blue phase liquid crystals under electrostriction. *Soft Matter* **18**, 3328–3334 (2022).
49. Fukuda, J.-i & Žumer, S. Field-induced dynamics and structures in a cholesteric-blue-phase cell. *Phys. Rev. E* **87**, 042506 (2013).
50. Fukuda, J.-i. Simulation of a cholesteric blue phase cell with large but finite thickness. *Front. Soft Matter* **2**, 1011618 (2022).
51. Pieranski, P., Dubois-Violette, E., Rothen, F. & Strzelecki, L. Geometry of Kossel lines in colloidal crystals. *J. Phys. Fr.* **42**, 53–60 (1981).
52. Alexander, G. P. & Yeomans, J. M. Numerical results for the blue phases. *Liq. Cryst.* **36**, 1215–1227 (2009).
53. Tiribocchi, A., Gonnella, G., Marenduzzo, D. & Orlandini, E. Switching dynamics in cholesteric blue phases. *Soft Matter* **7**, 3295–3306 (2011).
54. Li, X. et al. Mesoscale martensitic transformation in single crystals of topological defects. *Proc. Natl Acad. Sci. USA* **114**, 10011–10016 (2017).
55. Jin, H. M. et al. Soft crystal martensites: an in situ resonant soft x-ray scattering study of a liquid crystal martensitic transformation. *Sci. Adv.* **6**, eaay5986 (2020).
56. Liu, J. et al. Diffusionless transformation of soft cubic superstructure from amorphous to simple cubic and body-centered cubic phases. *Nat. Commun.* **12**, 3477 (2021).
57. Yamashita, A. & Fukuda, J.-i. Structure of twin boundaries of cholesteric blue phase I. *Phys. Rev. E* **105**, 044707 (2022).
58. Liu, Y. et al. Ultrafast pulse compression, stretching-and-recompression using cholesteric liquid crystals. *Opt. Express* **24**, 10458–10465 (2016).
59. Liu, Y. et al. Ultrafast switching of optical singularity eigenstates with compact integrable liquid crystal structures. *Opt. Express* **26**, 28818–28826 (2018).
60. Yoshida, H. et al. Bragg reflection band width and optical rotatory dispersion of cubic blue-phase liquid crystals. *Phys. Rev. E* **94**, 042703 (2016).
61. Chen, C.-W. & Khoo, I. C. Optical vector field rotation and switching with near-unity transmission by fully developed chiral photonic crystals. *Proc. Natl Acad. Sci. USA* **118**, e2021304118 (2021).
62. Lin, T.-H. et al. Data for “Directed crystalline symmetry transformation of blue-phase liquid crystals by reverse electrostriction.” zenodo <https://doi.org/10.5281/zenodo.12792108> (2024).
63. Guo, D.-Y., Feng, T.-M., Chen, W.-X., Zeng, P.-C. & Chen, C.-W. Codes for “Directed crystalline symmetry transformation of blue-phase liquid crystals by reverse electrostriction.” zenodo <https://doi.org/10.5281/zenodo.12792301> (2024).

Acknowledgements

This research was funded by Asian Office of Aerospace Research and Development (AOARD), Air Force Office of Scientific Research (AFOSR) —FA2386-20-1-4080 and FA2386-23-1-4124 (T.-H.L.); work at National Sun Yat-sen University was partially supported by National Science and

Technology Council of Taiwan—NSTC112-2223-E-110-004, NSTC113-2112-M-110-020-MY3, and NSTC113-2124-M-110-002-MY3 (T.-H.L.).

Author contributions

D.-Y.G. conceived and carried out the experiments with assistance from W.-X.Z., L.-Y.W., W.-M.G., L.-M.C., T.-M.F., H.-C.J., and C.-T.W.; C.-W.C. designed the Kossel fitting process; D.-Y.G., P.-C.C., T.-M.F., W.-X.Z., and C.-W.C. developed the codes; D.-Y.G., C.-W.C., and T.-M.F. performed the data analysis; T.-H.L., I.C.K., and T.J.B. supervised the project; I.C.K., C.-W.C., D.-Y.G., T.-M.F., and T.-H.L. prepared the manuscript.

Competing interests

The authors declare no competing interests.

Additional information

Supplementary information The online version contains supplementary material available at <https://doi.org/10.1038/s41467-024-51408-4>.

Correspondence and requests for materials should be addressed to Tsung-Hsien Lin or Iam Choon Khoo.

Peer review information *Nature Communications* thanks Yuzhan Li, and the other, anonymous, reviewer for their contribution to the peer review of this work. A peer review file is available.

Reprints and permissions information is available at <http://www.nature.com/reprints>

Publisher's note Springer Nature remains neutral with regard to jurisdictional claims in published maps and institutional affiliations.

Open Access This article is licensed under a Creative Commons Attribution-NonCommercial-NoDerivatives 4.0 International License, which permits any non-commercial use, sharing, distribution and reproduction in any medium or format, as long as you give appropriate credit to the original author(s) and the source, provide a link to the Creative Commons licence, and indicate if you modified the licensed material. You do not have permission under this licence to share adapted material derived from this article or parts of it. The images or other third party material in this article are included in the article's Creative Commons licence, unless indicated otherwise in a credit line to the material. If material is not included in the article's Creative Commons licence and your intended use is not permitted by statutory regulation or exceeds the permitted use, you will need to obtain permission directly from the copyright holder. To view a copy of this licence, visit <http://creativecommons.org/licenses/by-nc-nd/4.0/>.

© The Author(s) 2024